

# Soil Displacement Terramechanics for Wheel-Based Trenching with a Planetary Rover

Catherine Pavlov<sup>1</sup> and Aaron M. Johnson<sup>1</sup>

**Abstract**—Planetary exploration rovers are expensive, weight constrained, and cannot be serviced once deployed. Here, we explore one way to increase their capabilities while avoiding the cost, mass, and complexity leading to these issues. We propose to re-use the large wheel actuators for trenching and other digging operations, which will enable a range of missions such as sampling deeper layers of soil. We present a new, closed-form model of the soil displaced by an angled, spinning wheel to analyze the trenching potential of a driving strategy and inform the control of the wheel. The model is demonstrated with single wheel experiments under different driving conditions. The model suggests: that a deep trench does not require large tractive efforts; that the shape of the trench can be controlled; and that a rear wheel has a lower risk of entrapment when trenching than a front wheel. Ultimately this model could be used in a nonprehensile manipulation planning or learning algorithm to enable autonomous trenching.

## I. INTRODUCTION

This paper proposes a new terrain manipulation capability for planetary rovers that uses their existing wheels instead of adding a dedicated manipulator. Rover designs are constrained in mass, power, and complexity due to the launch costs and limited resources upon arrival. Therefore, adding a dedicated manipulator to interact with the environment is challenging and the final device is typically slow and weak. In this work, we explore what manipulation capabilities a wheeled rover can achieve without any additional hardware.

The primary actuators on most rovers are in the drive system. This creates an opportunity to produce significant manipulation forces by re-using the wheels for nonprehensile manipulation [1], that is, manipulation without a gripper or similar end effector [2–5]. Wheel-based manipulation could enable missions such as sampling soil at different depths, filling in a ditch or building a ramp to get over an obstacle, burying a cable, preparing a site for future manned missions, levelling a potential landing site, or recovering from a stuck wheel [6–8].

Here we focus on digging trenches because it is a simple behavior but still exposes many of the challenging modeling and control issues common to any of these behaviors. Preliminary experiments, shown in Fig. 1 and the video attachment, demonstrate that wheel-based trenching is in fact possible with a rover. The deepest of these trenches is 27mm, or 56% of the wheel radius, which would translate to a 150mm depth on Curiosity [9]. Extensive research has been conducted on the development of task-specific digging implements such



Fig. 1: K10 mini rover using its rear right wheel to trench. K10 mini is a microwave-sized rover from NASA Ames.

as bucket wheels for rovers [10–12], but not on the use of wheels to replace digging implements. Rover wheels have been used to dig during planetary missions on an ad hoc basis [6, 7], but robust tools enabling wheel-based digging have not yet been developed.

The key questions to enable these capabilities are:

- How is the size and geometry of a trench affected by driving (slip angle, slip ratio) parameters?
- Can we ensure the rover does not get stuck while driving?
- Does the choice of digging wheel affect platform mobility?

In this work we present a novel, first principles-based model of soil flow around a wheel (Sec. II), provide experimental validation of that model (Sec. III), and then use that model fused with an existing terramechanics model to answer the above questions (Sec. IV). In addition to providing these insights, this model can be used in the future to design motion controllers and a kinodynamic planner to enable autonomous trenching with a rover (as done for other nonprehensile behaviors, e.g. [13]).

## II. MODELING

Here we present a model mapping soil properties and rover driving parameters to deformed terrain geometry. The model consists of two parts: an existing terramechanics model to generate wheel-soil contact geometry and forces, and a newly developed soil flow model to generate the resulting soil deformation.

### A. Terramechanics Model

Many terramechanics models for wheeled vehicles exist for different settings [14–21], but all tend to be either fast

\* This work was supported by a NASA Space Technology Research Fellowship, as well as a NASA STTR grant, NNX16CA42P.

<sup>1</sup> Mechanical Engineering Department, Carnegie Mellon University, Pittsburgh, PA 15213, USA. {cpavlov, amj1}@andrew.cmu.edu

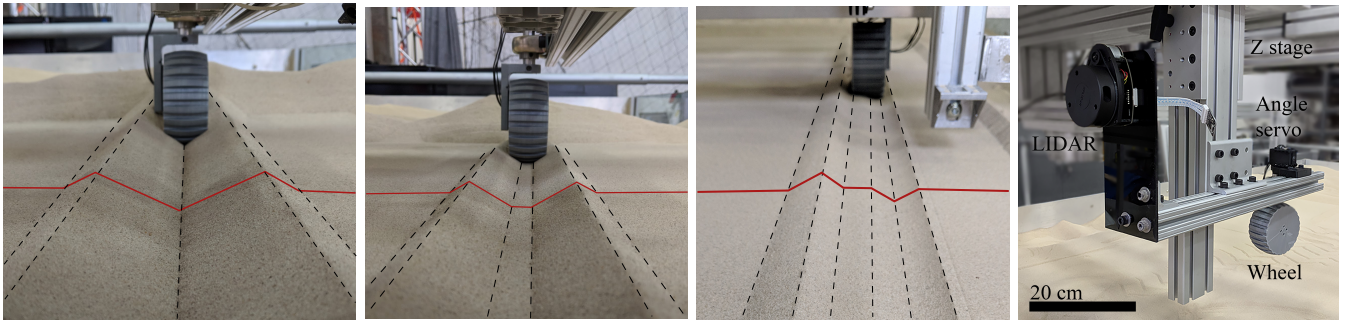


Fig. 2: Example trenches from the model validation experiments with a pointed bottom (left), flat bottom (center-left), and stepped geometry (center-right), along with the single-wheel testbed setup (right). For each trench, the wheel is lowered to a fixed sinkage ( $h_0$ ) and moves across level sand at a fixed slip ratio ( $s$ ) and slip angle ( $\beta$ ).

but inaccurate (e.g. neglecting resistance built by soil piled in front of a wheel), or accurate but slow (e.g. Discrete Element Methods, DEM, or Finite Element Methods, FEM). As one application for this model is to inform a kinodynamic planning or learning algorithm, evaluation must be very rapid. Resistive Force Theory provides more rapid force modeling than finite element methods at better accuracy than classical models, but fails at higher slip [21]. Of these, only the slower methods predict both forces on the wheel and resulting displacement of the soil [17–19].

Here, we use fast analytic fits to the key terramechanics equations developed in [14, 15], as in [20] (enabling rapid evaluation of wheel-soil interaction forces), and extend this model to predict soil motion during trenching. These equations are typically solved iteratively – by using quadratic fits, [20] is able to give approximate closed-form equations for the geometry of the wheel-soil interface (e.g. sinkage) as well as the forces and torques experienced by the wheel during driving. Following [20], we take the formulations for shear and normal stresses under a wheel as derived in [22] and use quadratic approximations to their forms, with coefficients stored in a lookup table, to rapidly evaluate the state of a driving wheel in a non-iterative manner.

### B. Soil flow model

Prior work on soil deformation has successfully predicted the shape of trenches for non-driven rolling wheels [23] and tailing piles behind wheels [24] using DEM methods. However, DEM methods are not suitable for integration into planning or learning algorithms due to their slow evaluation times. The model detailed here is entirely closed-form and evaluation is extremely rapid. The geometry of the wheel-soil interface, Fig. 3, is driven by the sinkage ( $h_0$ , as given by the terramechanics model from [20]) and driving parameters (slip angle,  $\beta$ , and slip ratio,  $s$ ).

When driving at steady state, all soil displaced by the wheel must flow around and back behind it. Displaced soil is either moved by plowing, where it flows around the sides of the wheel, or by entrapment in the grousers due to rotation of the wheel. The volume of sand in any unit length along the wheel’s tracks must be equal to the volume of sand per unit length in front of the wheel (with no compaction, an

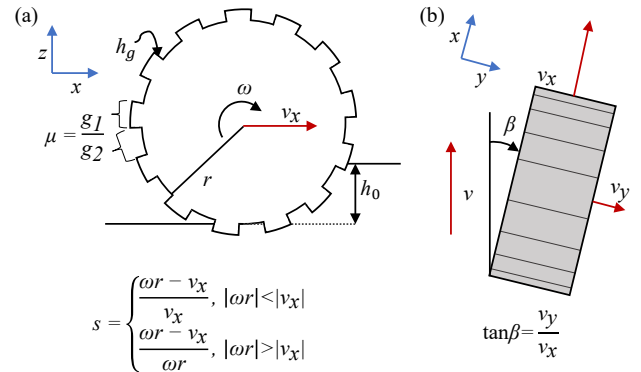


Fig. 3: Definition of key terramechanics values and wheel geometry. (a) shows the side profile of a wheel, and (b) shows a top-view.

assumption we test in Sec. III). As such, here we consider an infinitesimal slice of soil volume and refer to it as a planar soil area. At steady-state operation, all parameters that determine the planar soil area (e.g.  $\beta$ ,  $s$ ,  $h_0$ ) are constant. We classify the resulting trench shape into pointy bottomed, flat bottomed, [25], and stepped, as seen in Fig. 2.

To calculate the resulting profile, we use the constraints imposed by the angle of repose and by conservation of area [26]. The calculation, shown in Fig. 4, breaks the soil flow into four phases: 1) Soil Separation, 2) Grouser Soil Removal, 3), Inward Flow, and 4) Transported Pile Deposition.

1) *Soil Separation*: First, the area of soil interaction,  $A_{tot}$ , is assumed to be equal to the projected area of the wheel perpendicular to direction of travel, Fig. 4(a), as determined by the sinkage ( $h_0$ ), slip angle ( $\beta$ ), wheel radius ( $r$ ), and width ( $b$ ),

$$A_{tot} = A_{el}(r, h_0, \beta) + h_0 b \cos \beta \quad (1)$$

where  $A_{el}$  is the area of the semi-elliptical cross-section.

The sand is then separated into the piles that flow to the left and right of the wheel,  $A_{L1}$  and  $A_{R1}$ , respectively. We assume, without loss of generality, that the wheel is turned to the right. For large and small slip angles ( $\beta < 10^\circ$  or  $\beta > 80^\circ$ ), the soil is assumed to split evenly around the

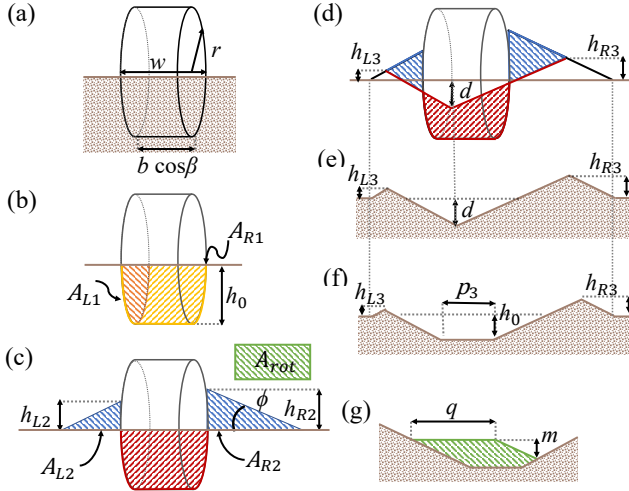


Fig. 4: Illustration of the soil flow model from behind the wheel. (a) The planar soil area. (b)-(c) The division of the soil into left and right piles around the wheel, with  $A_{L1} = A_{el}$  (in orange) (1).  $A_{rot}$  (green) is removed from the right section ( $A_{R1}$ , yellow). (d) Piles flowing back into the trench, with the red and blue areas equal. (e) The resulting trench with a pointed bottom. (f) The resulting trench with a flat bottom. (g) The formation of a step from  $A_{rot}$ .

wheel, creating a symmetric trench. For intermediate angles, the soil flow is assumed to split about the leading edge of the wheel, Fig. 4(b),

$$A_{L1} = A_{el}, \quad A_{R1} = h_0 b \cos \beta \quad (2)$$

2) *Grouser Soil Removal*: The soil flows past the wheel via two mechanisms: “plowed” sand, which flows around the left and right of the wheel, and “grouser transported” sand which is moved by the rotation of the wheel. The amount of soil transported by the rotation of the wheel is,

$$A_{rot} = 2\pi r \zeta h_g b \frac{\omega}{v_x}, \quad (3)$$

where  $\zeta$  is the volume fraction of the grousers (fraction of the wheel’s surface they make up,  $\mu$ , times the fraction of each grouser filled during trenching, empirically determined),  $h_g$  the grouser height,  $\omega$  the angular speed of the wheel in rotations/s, and  $v_x$  the forward velocity of the wheel as in (Fig. 3). This area is bounded by the amount of soil encountered by the grousers on the rotating surface of the wheel. For small angles ( $\beta < 10^\circ$ ), this soil is drawn equally from both the left and right piles, and is bounded by  $A_{tot}$ . For larger angles, it is drawn from the pile in the direction of rotation,  $A_{R1}$ . The right and left areas after the grouser transported sand is accounted for, in the low angle case, are  $A_{R2} = A_{L2} = (A_{tot} - A_{rot})/2$ , while for larger angles,  $A_{R2} = A_{R1} - A_{rot}$ ,  $A_{L2} = A_{L1}$ .

Determining where sand transported by rotation goes also depends upon the slip angle  $\beta$  of the wheel. For high angles ( $\tan \beta > b/(2\sqrt{2rh_0 - h_0^2})$ ), when the front and rear corners of the wheel align),  $A_{rot}$  is added to the opposite volume of plowed soil (so  $A_{L2} = A_{L1} + A_{rot}$ ). For intermediate and low angles,  $A_{rot}$  is set aside for now.

Soil piled on either side of the wheel, of area  $A_{R2}$  and  $A_{L2}$ , is placed initially in triangles with an angle  $\phi$ , the angle of repose of the soil, Fig. 4(c). The height of the initial soil piles is given by,

$$h_{L2} = \sqrt{2A_{L2} \tan \phi}, \quad h_{R2} = \sqrt{2A_{R2} \tan \phi}. \quad (4)$$

3) *Inward Flow*: The soil that was piled against the wheel then flows back into the trench behind the wheel, Fig. 4(d). The profile is assumed at first to have a pointy bottom ( $p_3 = 0$ ) with a final height of  $h_{R3}$  and  $h_{L3}$  on each side and a maximum depth of  $d$ , and is determined by solving a set of constraints,

$$h_{R3}^2 + h_{L3}^2 = d^2 - A_{rot} \tan \phi \quad (5)$$

$$2h_{R3} + 2h_{L3} + 2d = h_{R2} + w \tan \phi + h_{L2} \quad (6)$$

$$2h_{R3} + d = h_{R2} + \frac{w - b \cos \beta}{2} \tan \phi \quad (7)$$

where  $w = b \cos \beta + 2 \sin \beta \sqrt{2rh_0 - h_0^2}$  is the width of the wheel at its intersection with the soil surface. First, the area of the sand is preserved, (5). Next, the soil is assumed to move along the steepest gradient, meaning only inward flow, maintaining the width of disturbed terrain, (6). Finally, the deepest part of the resulting trench, of depth  $d$ , is assumed to align with the leading corner of the wheel, Fig. 4(e), (7).

The depth of the pointy bottom trench is then checked against the wheel sinkage  $h_0$  – the trench cannot be any deeper than the deepest part of the soil removed. If the predicted trench is too deep, then the trench has a flat bottom and the soil profile is recalculated with a known trench depth of  $h_0$ , as shown in Fig. 4(f).

4) *Transported Pile Deposition*: We now consider the soil transported by rotation,  $A_{rot}$ . The equations above give the final trench profile for the high angle case ( $\tan \beta > b/(2\sqrt{2rh_0 - h_0^2})$ ), as we have already taken the rotated soil into account.

In the low angle case,  $\beta < 10^\circ$ , the area transported by rotation  $A_{rot}$  is placed on the profile, centered along the wheel axis. The new profile then has a flat bottom, whose depth is increased until all of  $A_{rot}$  is accounted for.

In the intermediate angle case ( $\beta > 10^\circ$  and  $\tan \beta < b/(2\sqrt{2rh_0 - h_0^2})$ ), the soil is piled from the bottom up until either a stepped or flat-bottomed trench is created. A step with width  $q$  and height  $m$  is formed with area equal to  $A_{rot}$ , as seen in Fig. 4 (g). Soil is piled in a step with rightmost edge hitting where the right edge of each grouser meets the soil. It is piled until its height reaches the leftmost edge of the wheel, and is then expanded further to the right. If  $A_{rot}$  is large enough that the step runs into the right side of the trench, a flat bottom forms.

### III. MODEL INVESTIGATION

We demonstrate the effectiveness of the soil flow model presented in Sec. II with a set of trenching experiments conducted in the soft-soil testbed in Carnegie Mellon’s Field Robotics Center. As the approximated terramechanics model has already been validated in [20], only the soil flow model is evaluated.

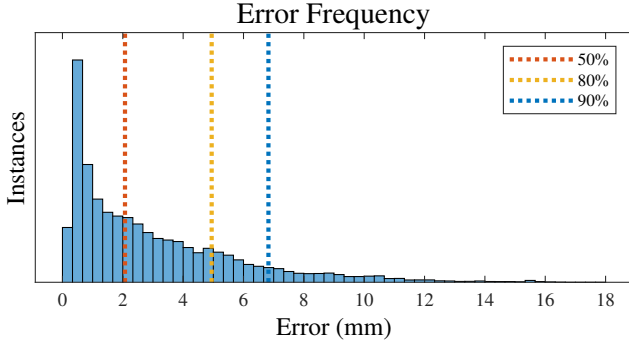


Fig. 5: Frequency of error in trench profile across all trials. 50% of points had less than 2.1 mm errors, 80% less than 4.9 mm, and 90% less than 6.8 mm

The goal of these experiments is to qualify the model as a whole by showing that the overall predicted soil profile closely matches that seen in experiments. In addition, some specific assumptions are investigated:

- Minimal soil compaction occurs
- The depth of trench follows the model
- The small and large slip angle transition points ( $\beta < 10^\circ$  and  $\beta > 80^\circ$ ) for soil division are reasonable.

In each trial, the wheel is set to a fixed sinkage ( $h_0$ ), slip angle ( $\beta$ ), and slip ratio ( $s$ ), and then driven through a prepared smooth soil bed in a straight line with a forward velocity  $v_x$  of 3 cm/s. Consistent soil preparation is achieved via jigs affixed to the testbed for loosening and leveling the sand. The resulting trench is imaged with a LIDAR scanner at 12 locations along its length, 5-10 cm apart, with each sample yielding a profile comprised of 300-400 unique points. The experimental setup is shown in Fig. 2 and the video attachment, and Table I contains relevant soil properties and wheel geometries. The wheel geometry was chosen to match the K10 mini rover, Fig. 1, which was used for preliminary trenching experiments.

LIDAR scans of the flat prepared surface have a standard deviation of 0.6 mm, which is less than the typical feature scale in these experiments. Calibration scans of alignment jigs are used to correct for rotation and offsets of the LIDAR scanner and testbed mounts. Experiments iterate over a representative range of wheel sinkages ( $h_0 \in \{5, 15, 25\}$  mm), slip ratios ( $s \in \{-1, -0.5, 0, 0.8, 0.9\}$ ), and slip angles

Sym.	Description	Value
$\phi$	Angle of repose [ $^\circ$ ]	29
$c$	Cohesion [Pa]	0
$n$	Sinkage exponent	1.0
$k_c$	Cohesive modulus [ $kN/m^{n+1}$ ]	0.9
$k_\phi$	Frictional modulus [ $kN/m^{n+2}$ ]	1523.4
$k$	Shear modulus [m]	0.025
$r$	Wheel radius [mm]	48.0
$b$	Wheel width [mm]	50.0
$h_g$	Grouser height [mm]	5.0
$\zeta$	Grouser volume fraction	0.1

TABLE I: Sand parameters (top) and rover parameters (bottom) used in this paper. Angle of repose is known for the sand used (Soil Direct #90), other values are typical as given in [20]. Rover parameters match that of the K10 mini.

( $\beta \in \{0^\circ, 22.5^\circ, 45^\circ, 67.5^\circ, 90^\circ\}$ ), for a total of 69 trenches and 828 sampled profiles<sup>1</sup>.

For each, the average error,  $\delta$ , of the trench model is evaluated by finding the average Euclidean distance from each measured point along the soil profile to the model profile generated with parameters listed in Table I, and then taking the average error in 0.8mm wide bins. Each bin is equally weighted in determining the overall  $\delta$  for the trench, to eliminate any bias arising from non-uniform distribution of sampled points. This error is given by,

$$\delta = \frac{1}{n_{bins}} \sum_{i=1}^{n_{bins}} \frac{1}{n_i} \sum_{j=1}^{n_i} |y_{actual,i,j} - y_{expected,i,j}| \quad (8)$$

The average error for each trench is reported in Table II, as is the median error between bins and the error on the maximum depth of the trench. Finally, these scans are also used to evaluate compaction, by comparing the net area of soil loss post-trenching to the area of soil disturbed by the wheel as predicted by the model,  $A_{tot}$ . A slice of the data for  $h_0 = 15$ mm is shown in Fig. 6.

*Model fit:* The qualitative trench fit was very good, with most qualitative trench shapes (flat vs. pointy, stepped or unstepped) successfully predicted by the model, Fig. 6. The average error over all trenches was 2.9 mm, with the maximum error at any individual point 18.2 mm. The frequency of error magnitudes can be seen in Fig 5.

The model fit was best for low and intermediate sinkages, and worst for high sinkages. Interestingly, the model performed well at high slip. This supports our quasistatic assumption, as the soil does not behave significantly differently at higher rotational speeds and thus any dynamic effects are small.

*Compaction:* The average compaction for all trenches was 4.29%, but this conceals more interesting behavior. Trench compaction was the most significant for trenches with  $\beta =$

<sup>1</sup>Note that the following trenches at the maximum sinkage were not completed due to excessive deflection of the test rig, indicating conditions where a rover would certainly get stuck:  $\beta = 67.5^\circ$  for  $s = -1$  &  $-0.5$ , and  $\beta = 90^\circ$  for  $s = -0.5$  through 0.9.

Trench Type	Avg. Error [mm]	Median Error [mm]	Depth Error [mm]	Compaction [%]
All trenches	2.9	2.1	3.5	4.29
$\beta = 0^\circ$	2.1	1.9	5.7	23.1
$\beta = 22.5^\circ$	3.3	2.3	4.0	7.19
$\beta = 45^\circ$	3.1	1.9	2.5	-9.3
$\beta = 67.5^\circ$	2.6	2.0	2.6	-3.02
$\beta = 90^\circ$	3.6	2.2	2.8	3.47
$s = -1$	3.5	2.3	3.4	5.76
$s = -0.5$	3.4	2.8	4.0	1.13
$s = 0$	3.3	2.1	4.1	17.12
$s = .8$	2.2	1.3	2.4	-2.48
$s = .9$	2.7	1.5	3.5	-1.0
$h_0 = 5$ mm	2.7	1.9	4.1	9.41
$h_0 = 15$ mm	2.7	2.1	3.6	1.9
$h_0 = 25$ mm	3.5	2.4	2.7	1.56

TABLE II: Quality of trench fit for all trials with the grousered wheel. Each row is an average over all other test conditions with the listed quantity held constant. Compaction is area change over  $A_{tot}$ .

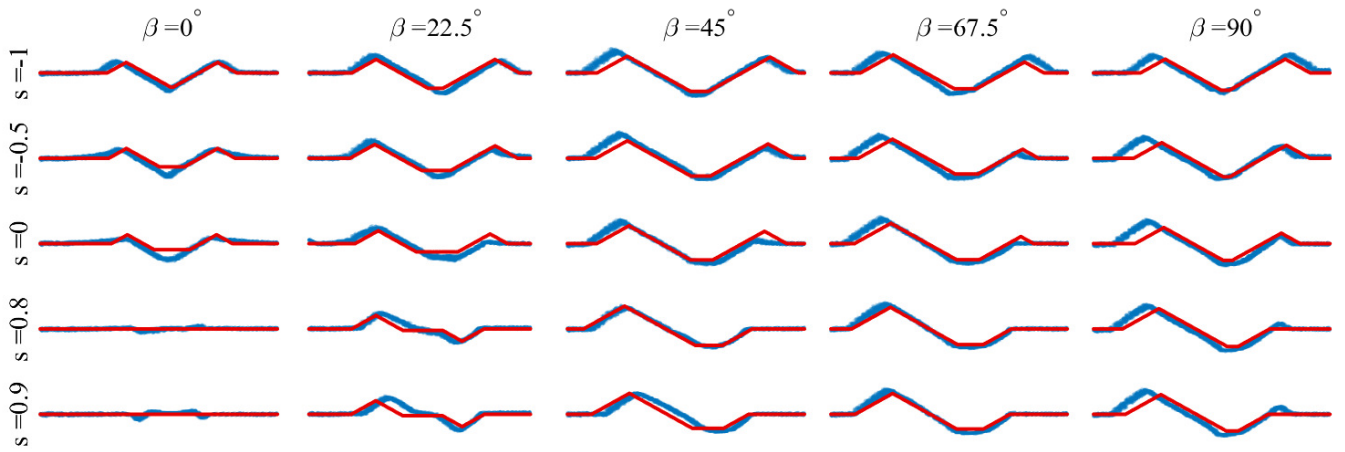


Fig. 6: Plots of measured (blue) and model-predicted (red overlay) trenches for varied slip angle and slip ratio at fixed sinkage of  $h_0 = 15\text{mm}$ . All 12 measurements of each trench are shown, showing the consistency of the trench. Note that the model captures the steps at the  $\beta = 22.5^\circ$  angle, the filled in trench at  $\beta = 0^\circ$  with high slip ratios, and the overall width and depth of most trenches.

$0^\circ$  and trenches with  $s = 0$ . In these cases, the wheel does not displace the soil as much as it rolls over, and exerts more force in the vertical direction, compacting it. At intermediate angles ( $\beta = 45^\circ, 67.5^\circ$ ) and very high slip ( $s = 0.8, 0.9$ ), the compaction is negative. This corresponds to the sand getting aerated by the wheel.

*Total depth:* The overall average error on the deepest part of the trench was comparable to the average error of the trench fit as a whole, as seen in Table II. The error on the maximum depth was about 3mm for most trenching configurations; however, the model was particularly good at predicting trench depth for trenches with intermediate or high  $\beta$  and particularly poor for low  $\beta$ .

*Small and large angle soil split rule:* The transition points in the soil division rule described in Sec. II-B occur at  $\beta = 10^\circ$  and  $\beta = 80^\circ$ . The angles tested on either side of these cutoffs ( $\beta = \{0^\circ, 22.5^\circ\}$ ,  $\beta = \{67.5^\circ, 90^\circ\}$ ) match the model well. Shifting the transition points to  $\beta = 25^\circ$  and  $\beta = 75^\circ$  such that the  $\beta = 22.5^\circ$  and  $\beta = 67.5^\circ$  trials are in the low and high angle regimes, respectively, gives worse fits. This suggests that the transition points do lie within the ranges  $[0^\circ, 22.5^\circ]$  and  $[67.5^\circ, 90^\circ]$ . However, more experiments are needed to refine these points.

#### IV. TRENCHING INSIGHTS

Numerical results based on this model were generated by testing different slip ratio and slip angle values using the parameters listed in Table I. These values were used to help answer the key questions outlined in Sec. I.

*Trench Shape:* A surprising variety of qualitatively distinct trench profiles emerge from the variation of slip angle, slip ratio, and sinkage. This model allows us to predict the shape of the trench, which may have a flat bottom or pointed bottom, smooth sides or a step, and piles of sand on both sides or just one side. We are able to select driving parameters (e.g.  $s$ ,  $\beta$ ) to achieve a desired trench geometry

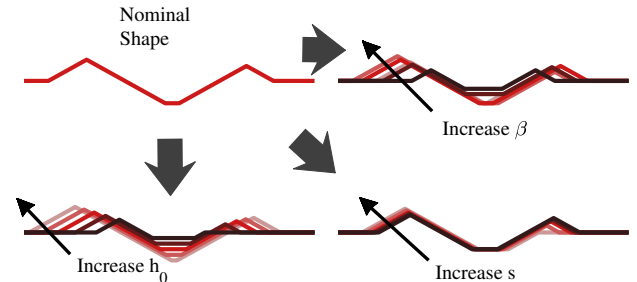


Fig. 7: Nominal trench shape for  $h_0 = 12\text{mm}$ ,  $\beta = 45^\circ$ , and  $s = 0$ , and the effect of varying each parameter individually from this case. Note that sinkage changes the shape of the trench's bottom, while slip angle and ratio affect the shape of the trench's sides.

– for example, one might choose to dig a trench with all soil piled to one side, so that a cable can then be laid in the trench and reburied with a single pass. Fig. 7 illustrates the effect of driving parameters on trench shape, and Fig. 8 shows the range of shapes possible for a single sinkage.

*Trench Depth:* Comparison of trench depth and wheel sinkage reveals that the deepest sinkage does not yield the deepest trench depth, as might be expected.

This can be seen in Fig. 9a, where the bottom surface shows the wheel sinkage ( $h_0$ ) and the top surface shows the resulting maximal trench depth ( $h_2$ ) at different slip angles and slip ratios. Note that depth is reported as distance from the original surface, and so deeper trenches are lower on the vertical axis. The regions where the surfaces intersect are conditions that yield a flat bottomed trench. The deepest sinkage occurs at around  $\beta = 0^\circ$  while the deepest trenches occur at around  $\beta = 50^\circ$  to  $\beta = 60^\circ$  for almost all slip ratios. Thus we can maximize trench depth without maximizing sinkage.

*Effect on driving:* With this model we can bound the allowable slip angles and slip ratios for a trenching wheel

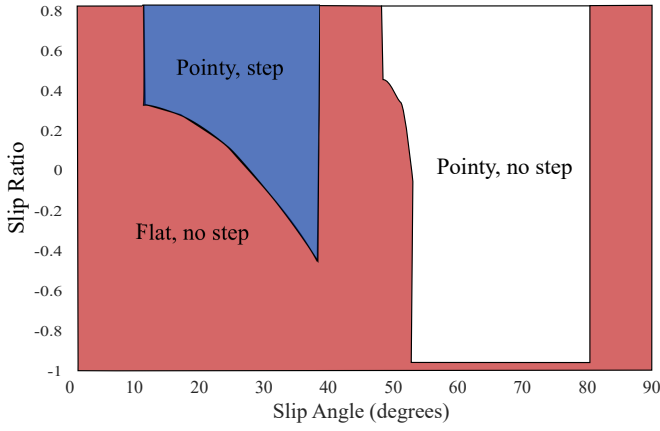


Fig. 8: Phase plot of trench shape for  $h_0 = 10\text{mm}$  generated from the soil flow model. Flat trenches have  $p_3 > 0$ , and stepped trenches have  $q > 0$ .

in order to avoid it getting stuck. The net tractive force is calculated by the terramechanics model outlined in Sec. II based on the driving parameters of the trenching and nontrenching wheels. Fig. 9b shows a plot of the trenching resistance of a wheel. By bounding the total tractive effort of the platform (e.g. three driving wheels plus one trenching wheel), we can obtain a set of  $(s, \beta)$  pairs for which the rover will not get stuck, and then select driving parameters to optimize trench depth.

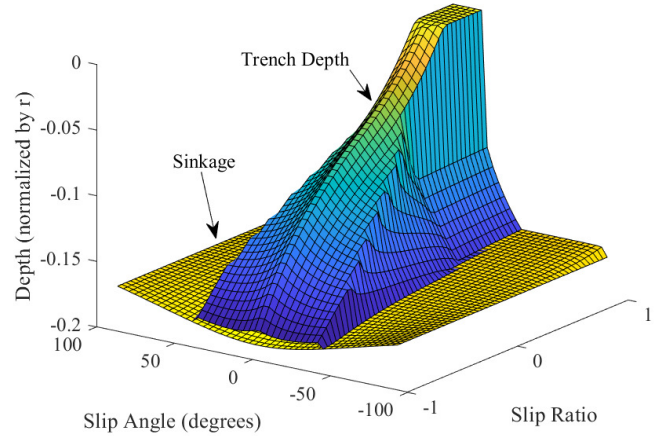
*Selection of trenching wheel:* In order to avoid getting stuck, it is better to trench with a rear rover wheel than a front wheel. Most rovers consist of a pair of rockers connected by an unactuated pivot mechanism. As such, one typical failure mode occurs when a single wheel of one rocker becomes entrapped in the sand, allowed to sink too deep by the free movement about the pivot. A parameter sweep of the terramechanics model shows that the net moment about a rover's rocker tends to pitch the front of the rocker down when one wheel is trenching, regardless of whether the front or back wheel is trenching. If the front wheel is trenching, this pushes the wheel deeper into the soil until the rover can no longer make forward progress.

This insight is supported by preliminary whole-rover experiments (shown in the video attachment), in which a trenching rover was much more likely to become trapped in the sand when trenching with front wheels than rear wheels.

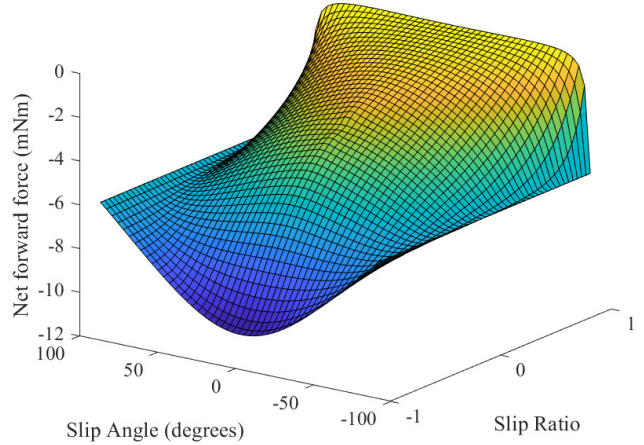
*Grouser Effect:* In preliminary tests it was observed that even wheels without grousers were capable of transporting soil by rotation. An ungrousered wheel can be used to dig in the same manner as a wheel with grousers, but the amount of soil moved by rotation is more difficult to predict, and likely depends on surface properties of the wheel as much as geometry. Further investigation in this area is needed.

## V. CONCLUSIONS

In this paper, we have proposed a model fusing a quadratic approximation to terramechanics models with first principle soil mechanics which describes the flow of soil around a trenching wheel. This model was demonstrated in a single-wheel testbed, and used to gain insight into how best to use



(a) Sinkage and trench depth



(b) Tractive effort

Fig. 9: Trench depth and sinkage (a) and trenching resistance (b) for different slip angles and slip ratios with an applied weight of 10N. Note that the deepest trenches occur at moderate slip angles with little sensitivity to slip ratio, while the tractive effort varies greatly with slip ratio.

the wheels of a rover to trench. The model shows that the rear wheel of a rocker pair should be used, it should be angled between  $50^\circ$  and  $60^\circ$  from the direction of driving for maximum trench depth, and the feasible control inputs can be bounded.

Future work will investigate model scaling to larger platforms, incorporation of soil transport for non-grousered wheels, and implementation of a kinodynamic planning or learning algorithm using this model. The ultimate goal is to enable the rover to autonomously combine different wheel-based terrain manipulation behaviors to achieve a higher level mission.

## ACKNOWLEDGMENTS

A preliminary version of some of this work was presented at the 2018 RSS Women in Robotics and Autonomous Space Robotics workshops [27] [28]. The K10 mini rover was graciously loaned by NASA Ames and Protoinnovations for this research. Thank you to David Wettergreen for the use of the soft-soil testbed.

## REFERENCES

- [1] M. Mason, D. Pai, D. Rus *et al.*, "A mobile manipulator," in *IEEE International Conference on Robotics and Automation*, vol. 3, 1999, pp. 2322–2327.
- [2] S. S. Srinivasa, C. R. Baker, E. Sacks *et al.*, "Experiments with nonholonomic manipulation," in *IEEE International Conference on Robotics and Automation*, vol. 2, 2002, pp. 2042–2047.
- [3] J. E. King, J. A. Haustein, S. S. Srinivasa, and T. Asfour, "Nonprehensile whole arm rearrangement planning on physics manifolds," in *IEEE International Conference on Robotics and Automation*, 2015, pp. 2508–2515.
- [4] K. M. Lynch and M. T. Mason, "Controllability of pushing," in *IEEE International Conference on Robotics and Automation*, vol. 1, 1995, pp. 112–119.
- [5] N. B. Zumel and M. A. Erdmann, "Nonprehensile two palm manipulation with non-equilibrium transitions between stable states," in *IEEE International Conference on Robotics and Automation*, vol. 4, 1996, pp. 3317–3323.
- [6] R. Sullivan, R. Anderson, J. Biesiadecki *et al.*, "Cohesions, friction angles, and other physical properties of Martian regolith from Mars Exploration Rover wheel trenches and wheel scuffs," *Journal of Geophysical Research E: Planets*, vol. 116, no. 2, 2011.
- [7] P. Leger, A. Trebi-Ollennu, J. Wright *et al.*, "Mars Exploration Rover surface operations: Driving Spirit at Gusev Crater," in *IEEE International Conference on Systems, Man and Cybernetics*, vol. 2, 2005, pp. 1815–1822.
- [8] J. Biesiadecki, E. T. Baumgartner, R. G. Bonitz *et al.*, "Mars Exploration Rover surface operations," *IEEE Robotics and Automation Magazine*, no. 1070-9932, pp. 63–71, 2006.
- [9] R. E. Arvidson, P. Bellutta, F. Calef *et al.*, "Terrain physical properties derived from orbital data and the first 360 sols of Mars Science Laboratory Curiosity rover observations in Gale Crater," *Journal of Geophysical Research E: Planets*, vol. 119, no. 6, 2014.
- [10] K. Skonieczny, D. Wettergreen, and W. Whittaker, "Advantages of continuous excavation in lightweight planetary robotic operations," *International Journal of Robotics Research*, vol. 35, no. 9, pp. 1121–1139, 2016.
- [11] L. L. Johnson and R. H. King, "Measurement of force to excavate extraterrestrial regolith with a small bucket-wheel device," *Journal of Terramechanics*, vol. 47, no. 2, pp. 87–95, 2010.
- [12] A. Wilkinson and A. Degennaro, "Digging and pushing lunar regolith: Classical soil mechanics and the forces needed for excavation and traction," *Journal of Terramechanics*, vol. 44, no. 2, pp. 133–152, 2007.
- [13] J. E. King, M. Cognetti, and S. S. Srinivasa, "Rearrangement planning using object-centric and robot-centric action spaces," in *IEEE International Conference on Robotics and Automation*, 2016, pp. 3940–3947.
- [14] S. Laughery, G. Gerhart, and R. Goetz, "Bekker's terramechanics model for off-road vehicle research," in *Ground Target Modeling and Validation Conference*, 1999.
- [15] J. Y. Wong, *Theory of Ground Vehicles*. John Wiley & Sons, 2008.
- [16] G. Meirion-Griffith and M. Spenko, "A modified pressure-sinkage model for small, rigid wheels on deformable terrains," *Journal of Terramechanics*, vol. 48, no. 2, pp. 149–155, 2011.
- [17] G. Ishigami, A. Miwa, K. Nagatani, and K. Yoshida, "Terramechanics-based model for steering maneuver of planetary exploration rovers on loose soil," *Journal of Field Robotics*, vol. 24, no. 3, pp. 233–250, 2007.
- [18] S. Taheri, C. Sandu, S. Taheri *et al.*, "A technical survey on terramechanics models for tire-terrain interaction used in modeling and simulation of wheeled vehicles," *Journal of Terramechanics*, vol. 57, pp. 1–22, 2015.
- [19] R. Krenn and A. Gibbesch, "Soft soil contact modeling technique for multi-body system simulation," *Lecture Notes in Applied and Computational Mechanics*, vol. 58, pp. 135–155, 2011.
- [20] Z. Jia, W. Smith, and H. Peng, "Fast analytical models of wheeled locomotion in deformable terrain for mobile robots," *Robotica*, vol. 31, no. 1, pp. 35–53, 2013.
- [21] C. Li, T. Zhang, and D. I. Goldman, "A terradynamics of legged locomotion on granular media," *Science*, vol. 339, no. 6126, pp. 1408–1412, 2013.
- [22] J.-Y. Wong and A. Reece, "Prediction of rigid wheel performance based on the analysis of soil-wheel stresses part i. performance of driven rigid wheels," *Journal of Terramechanics*, vol. 4, no. 1, pp. 81 – 98, 1967. [Online]. Available: <http://www.sciencedirect.com/science/article/pii/002248986790105X>
- [23] J. Hambleton and A. Drescher, "Modeling wheel-induced rutting in soils: Rolling," *Journal of Terramechanics*, vol. 46, no. 2, pp. 35–47, 2009.
- [24] M. Knuth, J. Johnson, M. Hopkins *et al.*, "Discrete element modeling of a mars exploration rover wheel in granular material," *Journal of Terramechanics*, vol. 49, no. 1, pp. 27 – 36, 2012.
- [25] E. T. Vincent, "Pressure distribution on and flow of sand past a rigid wheel: technical report," University of Michigan Research Institute, Tech. Rep., 1960.
- [26] R. A. Bagnold, *The Physics of Blown Sand and Desert Dunes*. Dover Publications, Inc., 1941.
- [27] C. Pavlov and A. M. Johnson, "Wheel-based trenching: Terramechanics of nonprehensile manipulation on planetary rovers," in *Robotics: Science and Systems Workshop on "Women In Robotics"*, Pittsburgh, PA, June 2018, Workshop poster.
- [28] —, "Wheel-based trenching: Terramechanics of nonprehensile manipulation for planetary rovers," in *Robotics: Science and Systems Workshop on "Autonomous Space Robotics"*, Pittsburgh, PA, June 2018, Workshop abstract.